Delay-Encoded Transmission and Image Reconstruction Method in Synthetic Transmit Aperture Imaging

Ping Gong, Michael C. Kolios, and Yuan Xu

***Abstract*—Synthetic transmit aperture (STA) imaging systems usually have a lower SNR compared with conventional B-mode ultrasound systems because only one or a small number of elements are selected for each transmission in STA. Here we propose delay-encoded synthetic transmit aperture (DE-STA) imaging to encode all the transmission elements to increase the SNR of the pre-beamformed RF signals. The encoding scheme is similar to the Hadamard encoding. However, in each transmission of DE-STA imaging, selected transmitting elements are delayed by a half period of the ultrasound wave relative to the rest transmitting elements, rather than using a pulse inversion as in the Hadamard encoding sequence. After all the transmission events, a decoding process in the temporal frequency domain is applied to the acquired RF signals to recover the equivalent traditional STA signals with a better SNR. The proposed protocol is tested with simulated data (using Field II) and experimental data acquired with a commercial linear array imaging system (Ultrasonix RP). The results from both the simulations and the experiments demonstrate increased SNR of pre-beamformed RF signals and improved image quality in terms of peak signal-to-noise ratio (PSNR), resolution and contrast-to-noise ratio compared with traditional STA. The lateral resolution (as assessed by a wire target) of DE-STA imaging is improved by 28% and the PSNR of the wire is increased by 7 dB, respectively, compared with traditional STA imaging. The proposed image reconstruction framework can also be extended to other transmission protocols.**

I. Introduction

Ultrasound imaging has been proven to be a safe, relatively simple and inexpensive, real-time imaging modality for soft tissues [1]. It has a good spatial resolution (on the order of hundreds of microns) and imaging depth (on the order of 10 cm) depending on the frequency range used. The conventional ultrasound imaging (B-mode) is one of the most commonly used modes, in which the RF signals are acquired after sending focused beams along various A-lines sequentially in time. A disadvantage of B-mode imaging is that the images are only optimally focused at one depth because of the single transmission focus [2]. Therefore, the spatial resolution of B-mode ultrasound images still needs improvement at locations outside the transmission focus. Synthetic transmit aperture (STA) imaging is an approach to solve this problem associated with B-mode ultrasound imaging. It is based on a software beamforming process, and focusing can be obtained at every point in the image in both transmit and receive [2]–[6].

Synthetic transmit aperture imaging has been widely used in different fields such as radar and sonar systems [7], nondestructive testing (NDT) [8], [9], seismic monitoring [10], and medical ultrasound imaging such as breast micro-calcifications detection [11] and flow estimation [12] because it provides images with high resolution and detectability. In STA imaging as shown in Fig. 1, an array of transmitters and receivers is typically used. Usually, an array element can serve as both a transmitter and then a receiver. Typically, each element of the transmitter array is excited consecutively. In each transmission, the active element emits a semi-spherical wave that propagates through a large image region and then all the receiving elements are used to acquire the RF backscatter signals, which can then be used to reconstruct a low-resolution image. Afterwards, all the low-resolution images can be combined coherently or incoherently to form a high-resolution image (see Fig. 1 in [2] for a detailed description of STA) [2]. We define the data obtained from the receivers in this transmission scheme as the traditional STA data.

Due to the fact that only one or a small number of elements are selected for the transmission, the low SNR is a major limitation in the STA system compared with the conventional B-mode imaging approach, where a focused beam is excited and one A-line is acquired at a time. Various approaches that involve using multi-element sub-apertures have been proposed to overcome the low SNR in STA [13]–[25]. One of them is synthetic aperture imaging using a virtual source element in transmit and dynamic focusing in receive [14], [15]. The virtual source is located at the transmission focal depth of a subarray. The multiple-element approach can increase the transmitting power and therefore, the SNR of the RF data. A similar technique, synthetic aperture sequential beamforming, has also been proposed which uses fixed focus in both transmit and receive to provide a more uniform resolution than the dynamic receiving focusing [18], [19].

The Hadamard spatial coding matrix has also been designed to solve the loss of SNR by spatially encoding the transmission elements and using its inverse for decoding the received RF data as shown in Fig. 2 [20], [21]. In this method, some array elements transmit a reference waveform, whereas the others transmit a phase inverted version of the reference waveform simultaneously. The transmission scheme can be described by a Hadamard matrix,

Manuscript received February 20, 2015; accepted July 6, 2015.

The authors are with the Department of Physics, Ryerson University, Toronto M5B 2K3, ON, Canada (e-mail: yxu@ryerson.ca).

DOI http://dx.doi.org/10.1109/TUFFC.2015.007005

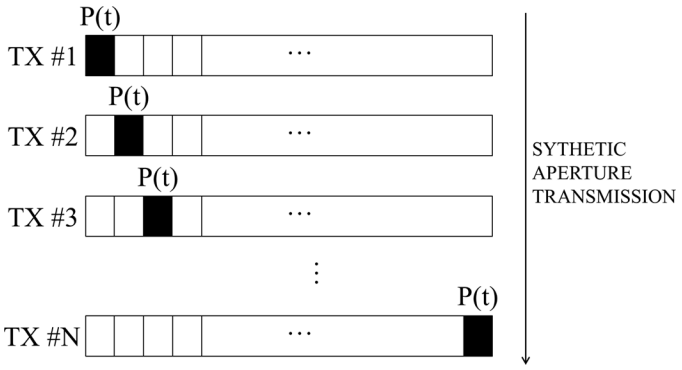

Fig. 1. Synthetic aperture ultrasound imaging transmission scheme. TX#1 to TX#N are N consecutive transmissions. In each transmission, only one element is excited with the same signal pulse P(t). Each square represents an element in the array, and the solid square in the figure denotes the active transmitting element.

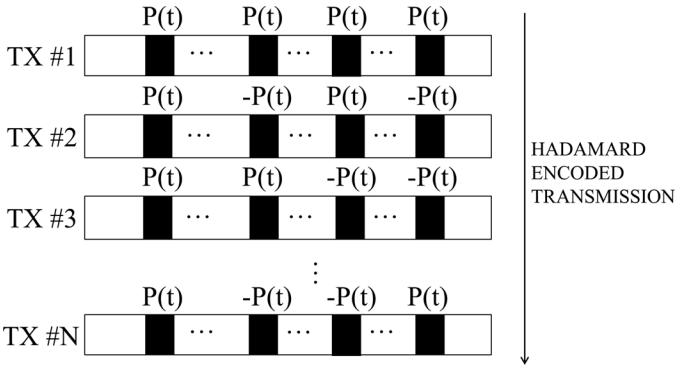

Fig. 2. Hadamard encoded transmission scheme. TX#1 to TX#N are N coded transmissions, and in each transmission, active elements are excited with combinations of pulses (P(t)) and phase inverted pulses (−P(t)) simultaneously according to the Hadamard matrix. The figure shows a size 4 Hadamard sequence as an example.

where 1 denotes reference pulse and −1 denotes negative/inverted pulse. More generally, multiple elements can be excited simultaneously with each excitation element transmitting different pulse sequences. After multiple transmissions, the backscatter signals received from all the transmissions can be processed to obtain the traditional STA data. The SNR of decoded RF signals could be increased by $\sqrt{I}$ times (I is the total number of active transmitters) compared with the traditional STA. A more sophisticated method utilizes the orthogonal Golay codes combining with Hadamard encoding for the spatio-temporal encoding to improve SNR further [22]. By using an orthogonal Golay set, the SNR of received data after decoding can be increased by $\sqrt{IS}$times (S is the temporal coding length).

Temporal encoding has also been applied in synthetic aperture imaging by using linear frequency modulated pulse (chirp) to increase the transmitted energy, and therefore increase the SNR while still retaining axial resolution [23], [26]. Chirped signals can also be combined with Hadamard encoding. However, Nikolov and Jensen found that this actually could degrade the image quality because nonlinear effects have been introduced into the medium via ultrasound propagation. Moreover, the implementation of chirped signals significantly increases the system complexity without proportionally matched improvement of image quality.

The Hadamard-based encoding protocols have common difficulties when being implemented in clinical devices. In many commercial scanners, the various elements of the array probe are driven by the same pulse sequence in one transmission, and only the timing or delay of the pulse sequence can be controlled/assigned for each individual element. The spatial coding proposed by Chiao et al. [20] requires that the various elements of the array probe are driven by two waveforms with opposite phase in one transmission. Therefore, the phase inversion proposed by Chiao et al. for the transmit electronics is not compatible with many commercial ultrasonic scanners (i.e., Ultrasonix RP, once the transmission sequence is designed, all the elements will be excited following the same sequence). In addition, any mismatch in the shape between the pulse and the phase inverted pulse may compromise its performance.

S-sequence encoded synthetic aperture imaging is an approach proposed to avoid the inverted pulses required for Hadamard encoding [24], [25]. The S-sequence encoding matrix is constructed by replacing 1 with 0, −1 with 1 of the Hadamard matrix, and then removing the first row and column of the newly constructed matrix. However, the injected power in each transmission will be halved, which reduces the SNR improvement.

Here we propose a new Hadamard based, delay-encoded synthetic transmit aperture (DE-STA) imaging protocol to spatially encode the transmission with half-period delay rather than with opposite polarity, to increase the SNR of the restored pre-beamformed RF data. The transmission of such an approach can be implemented in commercial scanners without significantly sacrificing the SNR improvement performance of Hadamard encoding. The proposed protocol was tested with the data from both Field II simulations and experiments.

II. Methods

A. Theory

Generally, we assume there are L transmission events in the data acquisition to form one high-resolution image (for example, $L = 4$ in Fig. 3; see Table I for nomenclature used in this paper). In each transmission, I elements (the same I elements for all the L transmissions) are excited with various delays, Δt_{li} ($l = 1{:}L$ and $i = 1{:}I$), relative to a reference time ($t = 0$), where Δt_{li} denotes the delay that is applied to the ith transmitting element in the lth transmission event. We define an L-by-I delay matrix $\mathbf{T}$ whose element is Δt_{li}. When there is no delay, Δt_{li} is 0; when there is a delay, Δt_{li} equals to half period [$(1/2f_0)$, f_0 is the central frequency of the ultrasound wave]. When multiple elements are excited together, the received signal equals the summation of the equivalent received signals

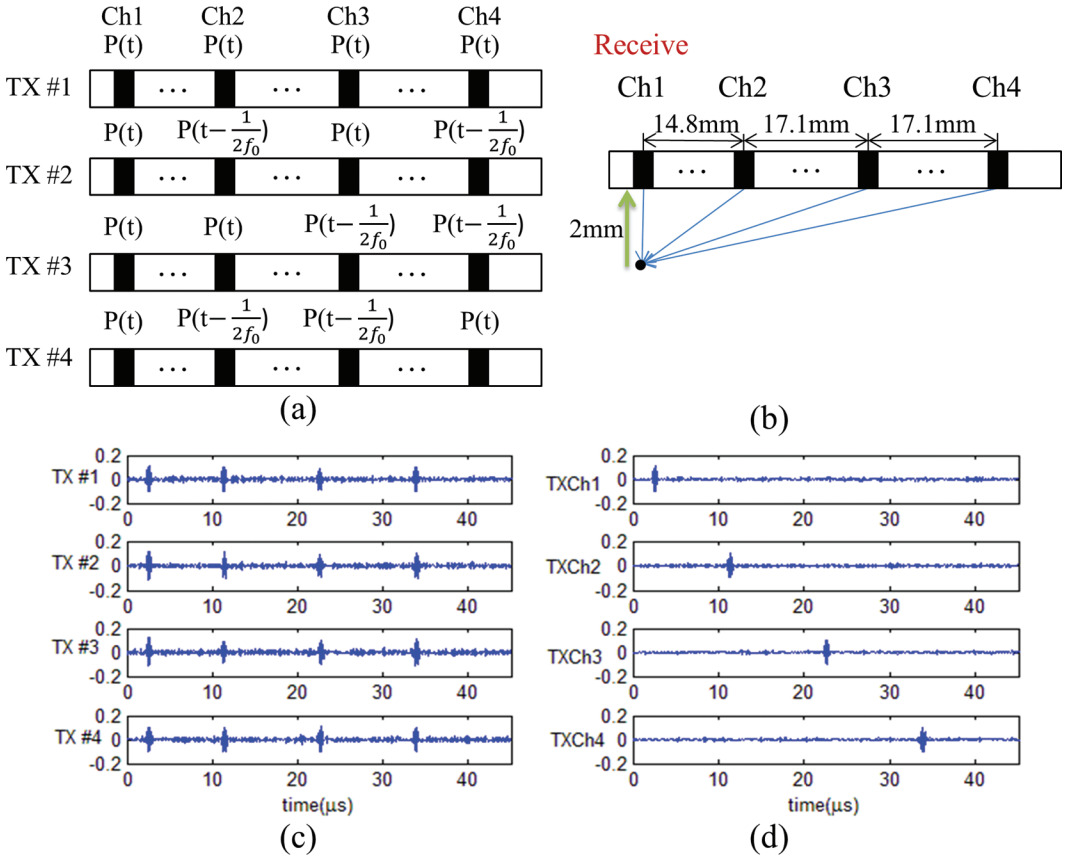

Fig. 3. The configuration and results of a numerical simulation with a point target and a 4-element array to illustrate DE-STA. (a) Waveform function of each transmission element in one of the total four transmission events (TX #*l*: *l*th transmission event). (b) Geometry of the simulation model. (c) Signals received by channel 1 in DE-STA imaging. (d) Decoded RF signals received by channel 1 when only one element is excited as in traditional STA imaging. (TXCh1: channel 1 is excited).

when the same set of elements are excited individually with the same corresponding delay. Therefore, for the *l*th transmission we have

$$\sum_{i=1}^{I} p_{ik}(t - \Delta t_{li}) = m_{lk}(t), \tag{1}$$

where $m_{lk}(t)$ is the RF signal in the DE-STA which is received by the kth ($k = 1{:}K$) receiving element in the lth transmission when multiple elements are excited together; and $p_{ik}(t)$ is the equivalent traditional STA signal, which is received by the kth receiving element when only the ith ($i = 1{:}I$) transmitting element is excited (while all the other imaging conditions are the same as in DE-STA).

According to the translation property of Fourier transform, applying a time-delay Δt_{li} to the received signal $p_{ik}(t)$ is equivalent to multiplying the signal spectrum $P_{ik}(f)$ by a factor of

$$A_{li}(f) = e^{-j2\pi f \Delta t_{li}}, \tag{2}$$

where f is any frequency in the spectrum. Therefore, after applying Fourier transform to both sides of (1), it can be transformed into the frequency domain at each frequency as

$$\sum_{i=1}^{I} A_{li}(f) P_{ik}(f) = M_{lk}(f), \text{ or} \tag{3}$$

$$\mathbf{AP} = \mathbf{M}, \tag{4}$$

TABLE I. List of Symbols.

Symbol	Description
A	Encoding matrix with elements of $A_{li}(f)$
$A_{li}(f)$	Elements of encoding matrix
D	Decoding matrix
f_0	Central frequency
$\mathbf{H}_n$	n-by-n Hadamard coding matrix
$i = 1{:}I$	Transmission element index
$k = 1{:}K$	Receiving element index
$l = 1{:}L$	Transmission event number
$m_{lk}(t)$	Time domain RF signal in the DE-STA which is received by the kth receiving element in the lth transmission event
$M_{lk}(f)$	Frequency spectrum of $m_{lk}(t)$
M	Matrix with elements of $M_{lk}(f)$, frequency-domain RF signal in the DE-STA
$p_{ik}(t)$	Equivalent traditional STA signal, which is received by the kth receiving element when only the ith transmitting element is excited
$P_{ik}(f)$	Frequency spectrum of $p_{ik}(t)$
P	Matrix with elements of $P_{ik}(f)$
Δt_{li}	Time delay that is applied to the ith transmitting element in the lth transmission event
T	Delay matrix with elements of Δt_{li}

where $M_{lk}(f)$ is the Fourier transform of signal $m_{lk}(t)$, and **A**, **P**, and **M** are matrices with elements of $A_{li}(f)$, $P_{ik}(f)$, and $M_{lk}(f)$, respectively. **A** is called the coding matrix which is constructed from the delay matrix **T**. Thus, the column index of **A** corresponds to a particular transmission element position, and each row includes the delays applied to all transmission elements in one transmission event. In the proposed DE-STA, $I = L$; otherwise, if $I > L$, **A** is highly ill-conditioned, pseudo-inverse, or another regularization method is needed to estimate the equivalent traditional STA data. Note that the coding matrix $A_{li}(f)$ depends on frequency. Eq. (4) can be solved to yield **P**, the spectrum of the traditional STA data. After that, the inverse Fourier transform of **P** can be used to produce the traditional STA data, $p_{ik}(t)$. Lastly, low-resolution images can be formed from the equivalent traditional STA data and then can be combined together to yield a high-resolution image.

The goal of decoding is to recover **P** from **M** in a stable way because **M** is usually contaminated by noise. To obtain **P**, one can multiply both sides of (4) with the decoding matrix $\mathbf{D} = \mathbf{A}^{-1}$. However the direct inversion may not be stable at some frequencies as explained below. Pseudo-inversion and other regularization techniques can be used instead of the direct matrix inversion to solve (4). After obtaining the $P_{ik}(f)$ for each frequency in the frequency spectrum of measured RF signals, an inverse Fourier transform is used to obtain $p_{ik}(t)$.

It is worth noting that when f equals to 0 or $2f_0$, the coding matrix will be a square matrix with all the elements equaling to 1, which cannot be inversed stably. To deal with this, the signal is processed by a band-pass filter to avoid the instable inversions around these frequencies.

Fig. 3 presents the configuration and results of a numerical simulation with a point target and a four-element array to illustrate the principle of DE-STA imaging. Each row of Fig. 3(a) depicts the waveform function of each transmission element in one of the total four transmission events, where TX #l means the lth transmission event. Fig. 3(b) presents the geometry of the simulation model. Each row of Fig. 3(c) shows the signals received by channel 1 in one transmission of DE-STA imaging. Each row of Fig. 3(d) displays the decoded RF signals received by channel 1 when only one element is excited as in the traditional STA imaging (TXCh1 means that channel 1 was excited). In Fig. 3, the decoding was implemented in the frequency range of 2.5 to 7.5 MHz with the central frequency at 5 MHz. Frequency components outside of this range were filtered by a Hanning window (2.5–7.5 MHz centered at 5 MHz). More discussions on Fig. 3 can be found in the Section IV.

B. Application to Ultrasound Imaging: Proposed Approach

To demonstrate that the delay-encoded transmission enables SNR improvement in pre-beamformed RF signals and improved image quality in synthetic transmit aperture imaging (STA), we have performed a series of simulations as well as experiments using the Ultrasonix RP (Ultrasonix, Richmond, BC, Canada). We will introduce the delay-encoded transmission based on the Hadamard matrix, the encoding and decoding methods, and the image reconstruction process for both simulations and experiments.

1) Implementation of the Delay-Encoded Transmission Following the Hadamard Matrix: In this section, we will describe how to construct the delay matrix **T** and the coding matrix **A** for the 128-channel (receive and transmit) system in our simulations and experiments. The delay matrix **T** is a 128-by-128 square matrix, which stands for $I = 128$ active transmitting elements in each excitation and $L = 128$ transmission events to acquire one complete set of data for one image. In each transmission, selected elements were delayed by a half period (the period was calculated at the central frequency of the transducer). We first constructed a Hadamard matrix of size 128, in which $H_{li} = 1$ indicates that no delay was added to the excitation of the ith element in the lth transmission and $H_{li} = -1$ indicates that a half period delay was added. The 128-by-128 Hadamard matrix $\mathbf{H}_{2^7}$ was constructed using Sylvester's construction as shown in (5).

$$\mathbf{H}_{2^N} = \mathbf{H}_2 \otimes \mathbf{H}_{2^{N-1}}, \tag{5}$$

for $N \geq 2$, where $\mathbf{H}_2 = \begin{bmatrix} 1 & 1 \\ 1 & -1 \end{bmatrix}$ and $\otimes$ denotes the Kronecker product. Once the Hadamard matrix of size 128-by-128, $\mathbf{H}_{2^7}$ is constructed, **T** can be obtained as

$$\mathbf{T} = (1 - \mathbf{H}_{2^7})\frac{t_d}{2}, \tag{6}$$

where $t_d = (1/2f_0)$ (half a period).

2) Generating the Simulated RF Data with Field II for B-Mode, STA, and DE-STA: The 2-D simulations were performed using the Field II program [27], [28]. First, we computed the traditional STA signals, which contained the backscatter signals of all receiving channels when each element was excited individually in a traditional STA scan. Then they were delayed according to the delay matrix **T** and summed to yield the simulated DE-STA signals. We also simulated B-mode imaging for the same phantom, probe, and imaging configuration. We considered a 4-cm-wide linear array probe with 128 elements excited with a 5-MHz central frequency. The received signals were sampled at 40 MHz and no attenuation was considered in the simulations. The location of the focus in the B-mode image was set at a depth of 3 cm in the phantom. The transducer array was simulated with 0.28 mm width, 0.02 mm kerf, and 1540 m/s speed of sound, exactly following the array used in experiments.

The simulated medium was a 40 mm × 10 mm × 40 mm (lateral × elevational × axial), which had a total of

200,000 point scatters. The phantom included a hyper- (on the left) and a hypo-echoic inclusion (on the right) with the same diameter of 12 mm. Both inclusions were centered at 30 mm away from the phantom top surface. In the background as well as in the hyper-echoic inclusion, the spatial distribution of the scatters was uniform and their scattering amplitude followed a zero mean Gaussian distribution. The standard deviation of the amplitude distribution of the scatters inside the hyper-echoic inclusion was 10 times that of the background and the hypo-echoic inclusion had no scatters. The probe was 5 mm away from the phantom surface.

To simulate the DE-STA signals, we first used Field II to generate the traditional STA data and then used (1) to yield DE-STA signals. To generate the DE-STA signals in the lth ($l = 1$–128) transmission, a half-period delay (100 ns) was applied to the traditional STA RF signals, which corresponded to the transmission channels that should be delayed according to the lth row of the delay matrix $\mathbf{T}$. Then the signals of the kth ($k = 1$–128) receiving channel in the lth transmission of DE-STA were obtained by summing the 128 kth receiving channel signals (after being delayed according to the lth row of the delay matrix $\mathbf{T}$) from the 128 transmissions of the traditional STA, as in (1). This process was repeated 128 times for the 128 different transmissions ($l = 1$–128) of one DE-STA process.

White Gaussian noise with a SNR of -10 dB was first applied to the traditional STA data. The SNR was calculated using (7):

$$\mathrm{SNR}_{\mathrm{dB}} = 20\log_{10}[\mathrm{norm(signal)}/\mathrm{norm(noise)}]. \quad (7)$$

Then, the noise with the same energy [norm(noise)] was added to the DE-STA signals assuming that both traditional STA and DE-STA have the same source of noise, such as electronic noise. Afterwards, all the RF data were processed by a fourth-order Butterworth filter with the pass-band ranging from 3.5 to 6.5 MHz (the frequencies corresponding to half-maximum of the filter). Then the resultant SNR after the filtering was 0 dB in traditional STA.

The decoding algorithm was implemented in Matlab R2012b (The MathWorks Inc., Natick, MA, USA) as explained in Section II. The received RF signals in DE-STA were first transformed into frequency domain using fast Fourier transform to obtain matrix $\mathbf{M}$. The decoding matrix $\mathbf{D}$ was obtained by direct inversion. The frequency spectrum of decoded RF signals $\mathbf{P}$ was calculated using $\mathbf{P} = \mathbf{DM}$. Lastly, the signal in time domain was computed by applying inverse Fourier transform function to $\mathbf{P}$. The decoding process was implemented in the frequency range of 2 to 9 MHz, in which the above filter has a nonzero weight. This band-pass filter was also applied to the traditional STA pre-beamformed data for fair comparison of the image qualities between STA and DE-STA images, both of which were obtained using the standard delay and sum reconstruction method in STA [2] with dynamic apodization.

C. Experimental Acquisition Setup

The experimental RF data were acquired using an Ultrasonix RP research platform equipped with the parallel channel acquisition system SonixDaq (Ultrasonix). The ultrasound probe was L14–5, which was a 4-cm-wide flat linear array probe with 128 elements that could be used as both transmitters and receivers. The transmission scheme was controlled by Texo, a development toolkit provided by Ultrasonix that allows for lower level control of ultrasound system using a program written in C/C++. The central frequency of the transducer was 5 MHz, and data were sampled at 40 MHz. The tissue-mimicking phantoms were made of degassed water (93.85% of total weight), gelatin powder (4.69%), polyethylene oxide (scatter) (1%), and formaldehyde (0.46%). In the background of the phantoms, the scatter concentration was 1% of the total weight, whereas inside the hyper-echoic inclusions the scatter concentration was twice that and the hypo-echoic inclusions had no scatters.

RF data were acquired in B-mode (used as a standard reference), traditional STA, and DE-STA for each phantom with exactly the same set of system parameters (such as the voltage levels for the transmission pulses). The transducer was fixed on the top of the phantom surface to ensure that images were taken from exactly the same section. The beamformed signals were processed by Hilbert transform followed by the logarithm compression and were then displayed as log-envelope images. The decoding and reconstruction processes for the experiment data were the same as those described in the above section on the numerical simulations.

The experimental DE-STA data were acquired from three different phantoms for different perspectives, which we defined as Phantom 1, Phantom 2, and Phantom 3. Phantom 1 was a 4 cm by 4 cm square phantom that contained both a hyper- (on the right side) and a hypo-echoic (on the left) inclusion with a diameter of 1.2 cm, and three wire inclusions of 0.5 mm diameter. Phantom 2 was a 4 cm by 6 cm phantom that contained 3 hypo-echoic inclusions with a diameter of 1.6, 1.2, and 0.7 cm, from the top to the bottom of the phantom, respectively. Phantom 3 was a 4 cm by 6.4 cm phantom that contained three 1.2-cm-diameter hyper-, hypo-, and hyper-echoic inclusions from the top to the bottom and also 4 wire phantoms located at approximately the depth of 5 cm.

III. Results

A. Simulation Results

Fig. 3(c) shows the DE-STA RF signals in the simplified simulation model with a point target and a four-element array. The panels from the top to the bottom correspond to DE-STA RF signals received by channel 1 in the first, second, third, and the fourth DE-STA transmission, respectively. In any transmission event, there are

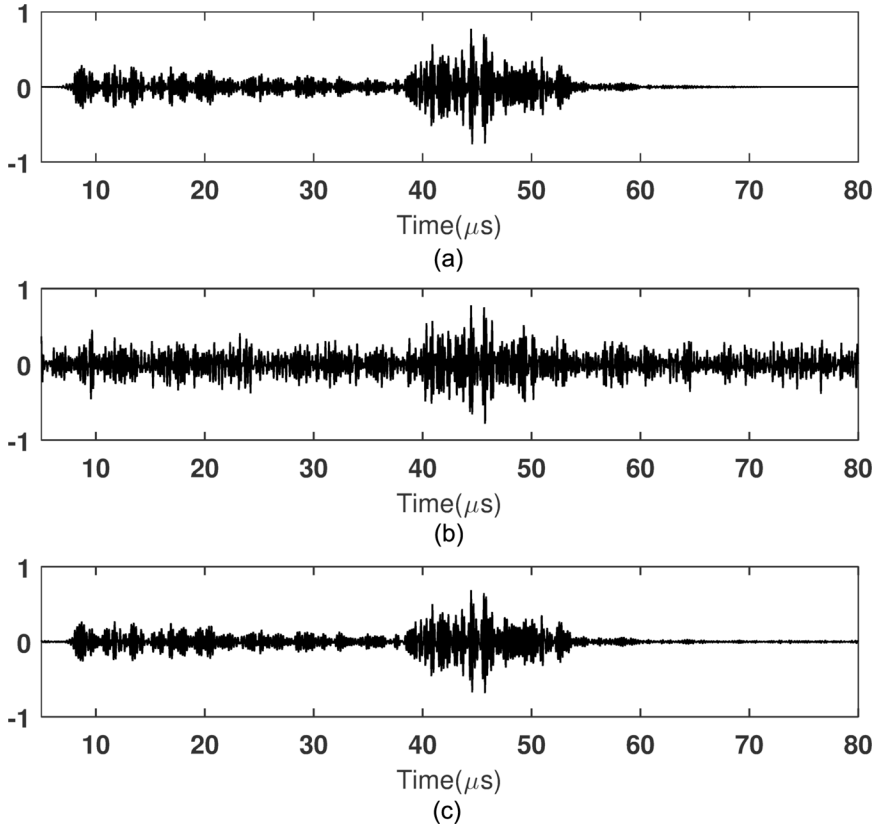

Fig. 4. Plots of the simulated raw RF signal obtained from (a) traditional STA imaging without noise, (b) traditional STA imaging with noise, and (c) the restored traditional STA by decoding the DE-STA signals with the same level of noise as in (b).

four pulses in one RF signal and they correspond to the four transmission elements. Fig. 3(d) shows the decoded RF signals. The panels from the top to the bottom correspond to the recovered RF signals received by channel 1 if channels 1, 2, 3, and 4 were excited individually as in traditional STA. There is only one pulse in a RF signal in each transmission. The SNR in the signals before and after decoding are 3.79 and 7.19, respectively, which can also be visualized by comparing the signals in Figs. 3(c) and 3(d). The amplitude of noise was reduced with the signal amplitude remaining almost the same. Therefore, the SNR of RF signals has been improved by 1.89 times by DE-STA technique.

Fig. 4 shows the results of the simulation with Field II. Fig. 4(a) shows the line plot of a typical pre-beamformed RF signal in the traditional STA without adding noise. The signal was received by the 30th element at the transmission of the 30th element in Field II. Fig. 4(b) shows the same signal after adding 0-dB bandpassed noise. As introduced in Section II, we added the same level of noise to the simulated DE-STA signals. Fig. 4(c) is the restored traditional STA signal by decoding the noisy raw DE-STA signals. The signal in Fig. 4(c), decoded from the DE-STA signals, is similar to the noiseless STA signal in Fig. 4(a) and has a better SNR than the noisy traditional STA signal in Fig. 4(b). As described in Section II-B-2, the resultant SNR in Fig. 4(b) is 0 dB. The SNR of the signal [Fig. 4(c)] restored from the DE-STA signals is 18 dB. Therefore, the pre-beamformed RF SNR has been increased by 18 dB (~8 times) in DE-STA over the traditional STA.

The improvement of SNR in DE-STA for pre-beamformed RF signals in Figs. 3 and 4 over the traditional STA is 1.89 times and 8 times, respectively. The SNR improvement is close to the theoretical limit, $\sqrt{I}$ (I is the total number of transmitters, i.e., 4 for the simulation in Fig. 3 and 128 for the simulation in Fig. 4). The actual values are slightly lower than the theoretical ones. This is because the optimum SNR improvement occurs only at the central frequency f_0.

Figs. 5(a) and 5(b) show the beamformed log-envelope images in conventional B-mode imaging and reconstructed traditional STA imaging, respectively, when there is no noise added to the RF data. Figs. 5(c) and (d) are the traditional STA and DE-STA images under the same amount of noise, respectively. The DE-STA provided an image with a better SNR than that in the traditional STA. The DE-STA image (d) also agrees well with the corresponding B-mode image (a) and the STA image (b) without adding noise to the RF data.

B. Experimental Results

Fig. 6 shows the images (the top row) and line plots (the bottom row, at the location of the horizontal white lines through the wire as indicated by the white arrows) in B-mode imaging (a), traditional STA imaging (b), and

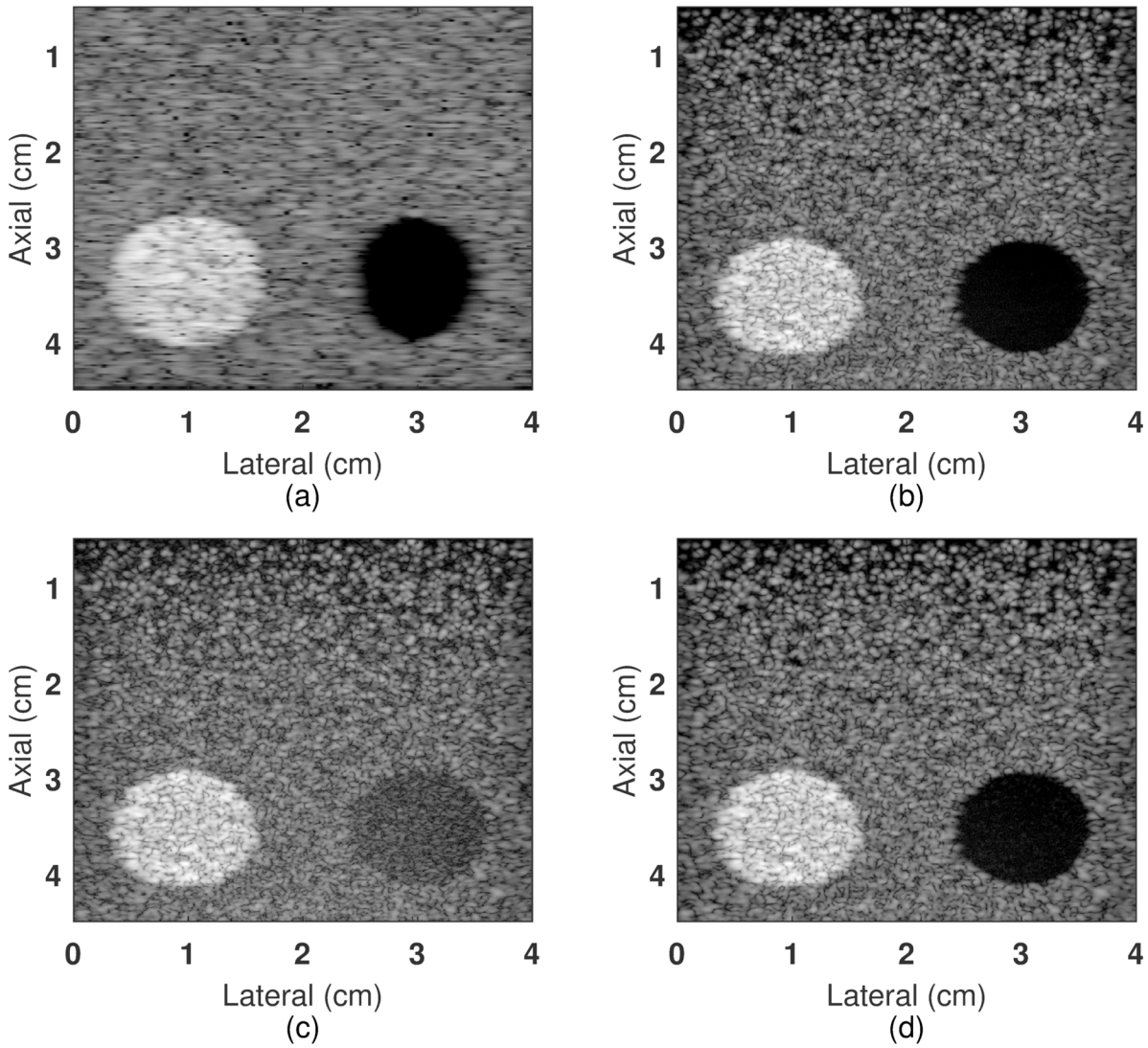

Fig. 5. Simulated log-envelope beamformed images obtained in (a) B-mode imaging, (b) traditional STA imaging without adding noise, (c) traditional STA imaging with noise, and (d) DE-STA imaging with the same amount of noise in STA raw RF signals as in (c). The dynamic ranges are (a) 160 dB; (b), (c), and (d) 60 dB.

DE-STA imaging (c) of Phantom 1. The measured spatial lateral resolution, peak signal to noise ratio (PSNR) of the wire target, and contrast to noise ratio (CNR) values of the hyper-echoic inclusion were used to compare the image quality of the various imaging methods (Table II). The image spatial resolution, PSNR, and CNR of the hyper-echoic inclusion in DE-STA were improved over those of the traditional STA image. Both the circular inclusions and the wire targets were better detected in the DE-STA image than the STA image. The bright dots inside the hypo-inclusion (probably due to air bubbles) can also be clearly seen after DE-STA reconstruction. The line plots (second row, Fig. 6) further demonstrated that the spatial resolution and PSNR from the wire inclusion (denoted by the arrows) have been enhanced: the lateral resolution [assessed by the full width at half maximum (FWHM)] in DE-STA was improved by 28% and the PSNR was increased by 7 dB, compared with the traditional STA image. The DE-STA image also provided best contrast property as assessed by the CNR of the hyper-inclusion.

Fig. 7 shows the images (the top row) and line plots (the bottom row, along the vertical white lines) in B-mode imaging (a), traditional STA imaging (b), and DE-STA imaging (c) of Phantom 2. Both the phantom images and the line plots of DE-STA imaging present a better contrast and spatial resolution than those of the traditional STA imaging. The smallest inclusion, which was located at around the depth of 5.5 cm, demonstrated that even for the inclusion which was far from the transducer surface, high resolution can still be obtained in DE-STA image due to the improved SNR of the pre-beamformed RF signals. Detailed CNR comparison of traditional STA and DE-STA images from 2nd and 3rd hypo inclusions are shown in Table III.

Fig. 8 shows the images (the top row) and line plots (the bottom row, along the vertical white lines) in B-mode

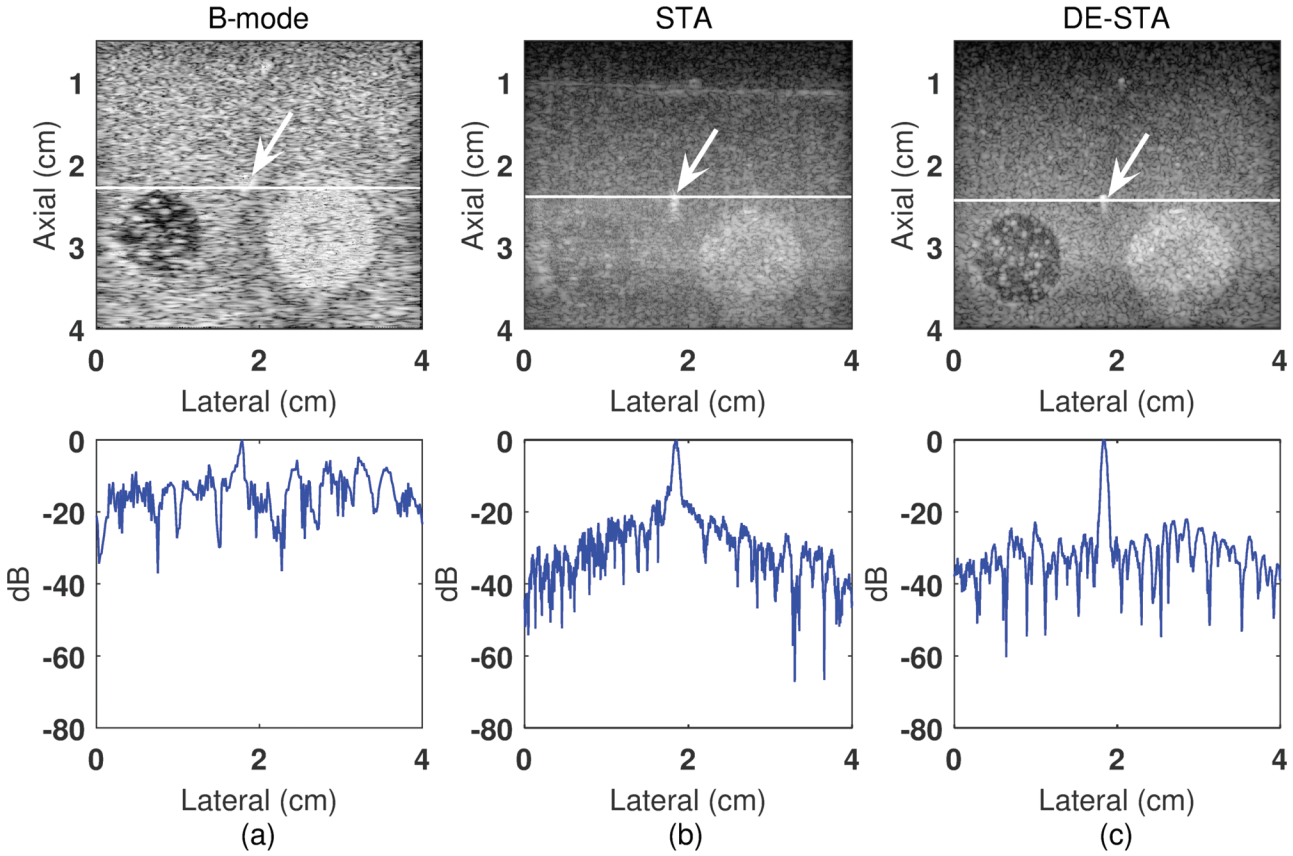

Fig. 6. Experimental log-envelope beamformed images obtained in (a) B-mode imaging, (b) traditional STA imaging, and (c) DE-STA imaging. Top row: phantom images. Bottom row: lateral line plots at the depth of 2.4 cm. The white line indicates the position of line plots in the images. The dynamic ranges are (a) 40 dB; (b) and (c) 80 dB.

imaging (a), traditional STA imaging (b) and DE-STA imaging (c) of Phantom 3. The B-mode image displays a severe shadow below the first hyper inclusion (in both log-envelope image and axial line plot), which leads to the indiscernibility of the other two inclusions. However, the STA and DE-STA images were less affected from the shadow brought by the first inclusion. The DE-STA image gave a better contrast for the hypo inclusion underneath the first hyper inclusion than those of the B-mode and the traditional STA images.

IV. Discussion

The proposed DE-STA was demonstrated to improve the SNR of pre-beamformed RF signals and, therefore, the image qualities over the traditional STA in terms of spatial resolution, PSNR, CNR, and detectability of inclusions. At the central frequency of the transducer array, DE-STA is equivalent to the spatial coding with Hadamard matrix [20], [21]. If we consider an ultrasound pulse as a sinusoidal wave train, shifting the wave train by a half period is a rough approximation of inverting the wave train. Therefore, we can consider DE-STA as an approximation of the spatial coding that occurs with the Hadamard matrix. Because the spatial coding with the Hadamard matrix has been shown to improve the SNR of RF signals in ultrasound imaging, it is not surprising that DE-STA imaging can improve the SNR of RF data.

TABLE II. PSNR and FWHM of the Point Target and CNR of the Hyper-Echoic Inclusion in Conventional B-mode, Traditional STA and DE-STA Images, Respectively, in Fig. 6.

Mode	PSNR [dB]	$FWHM_{lat}$ [mm]	CNR (hyper)
B-mode	16.7	1.00	0.9186
STA	31.0	0.72	1.1725
DE-STA	38.0	0.60	1.4229

The spatial resolution was significantly improved in DE-STA over STA imaging, which was demonstrated by significantly reduced size of both the wire phantoms and the speckles in all DE-STA images. Furthermore, the bright dots in the hypo-inclusions, which might be caused by air bubbles were also better detected in DE-STA images. These improvements are due to the fact that DE-STA imaging can increase the SNR of pre-beamformed RF signals by multi-element transmission to achieve the highest potential spatial resolution in traditional STA imaging. The B-mode images at the transmit focus could not yield the same resolution as the STA (DE-STA) images (e.g., Fig. 5). This is because the active aperture of B-mode imaging to form each A-line focusing at 3.5 cm depth was 32 elements to simulate the Ultrasonix RP hardware limit, whereas in STA or DE-STA images, the active aperture at the same depth was the whole array (128 active elements).

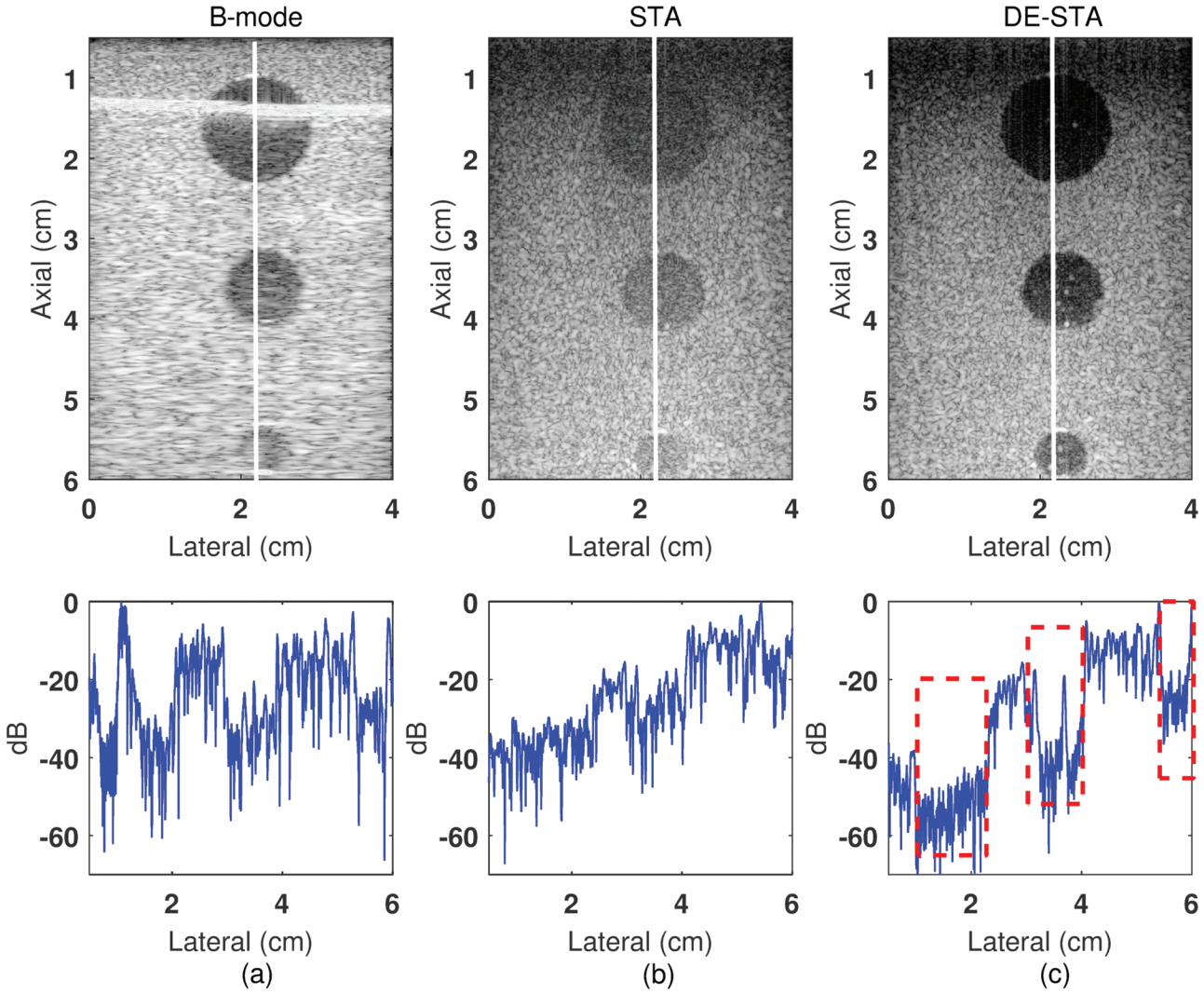

Fig. 7. Experimental log-envelope beamformed images obtained in (a) B-mode imaging, (b) traditional STA imaging, and (c) DE-STA imaging. Top row: phantom images. Bottom row: axial line plots at 2.25 cm (indicated by vertical white line). The dynamic ranges are (a) 40 dB; (b) and (c) 60 dB. Three dashed squares on axial line plots indicate the position of the three hypo inclusions.

DE-STA imaging was also shown to be least sensitive to the shadowing effect (Fig. 8). The B-mode image was acquired by sending focused beams sequentially. Consequently, the upper inclusion blocked the beam and therefore shadowed inclusions under it. In STA and DE-STA imaging, the upper inclusion can only block the beams associated with the transmission elements right above the upper inclusion, whereas other elements can still transmit ultrasound to the area below the upper inclusion. Even though shadowing effect in clinical ultrasound imaging can provide useful diagnostic information, when the region of interest is right under a highly attenuating object (Fig. 8), we think DE-STA imaging is still a useful approach to reduce the shadowing effect. The hypo-echoic inclusion in the middle of Fig. 8 can be visualized better in DE-STA image than the STA image due to the much improved RF SNR. Therefore, DE-STA approach can minimize shadowing effect.

TABLE III. CNR OF THE 2ND AND 3RD HYPO INCLUSIONS IN CONVENTIONAL B-MODE, TRADITIONAL STA, AND DE-STA IMAGES, RESPECTIVELY, IN FIG. 7.

CNR	2nd hypo	3rd hypo
B-mode	1.8824	0.7913
STA	0.7539	0.4158
DE-STA	2.4973	1.9246

The data acquisition speed in DE-STA imaging can be as fast as B-mode imaging and STA imaging because all of them have the similar transmission numbers (~128). The time it took for image processing and reconstruction in DE-STA imaging were 1 and 10 min, respectively, on a DELL OptiPlex 790 computer using Matlab R2012b software. The decoding processes for each frequency and each receiving channel are independent, which makes the process amendable to parallel programming. After decoding, the image reconstruction in traditional STA imaging can be implemented in real time [29], [30]. Therefore, future work may focus on the optimization of DE-STA imaging to speed up the decoding process and image reconstruction.

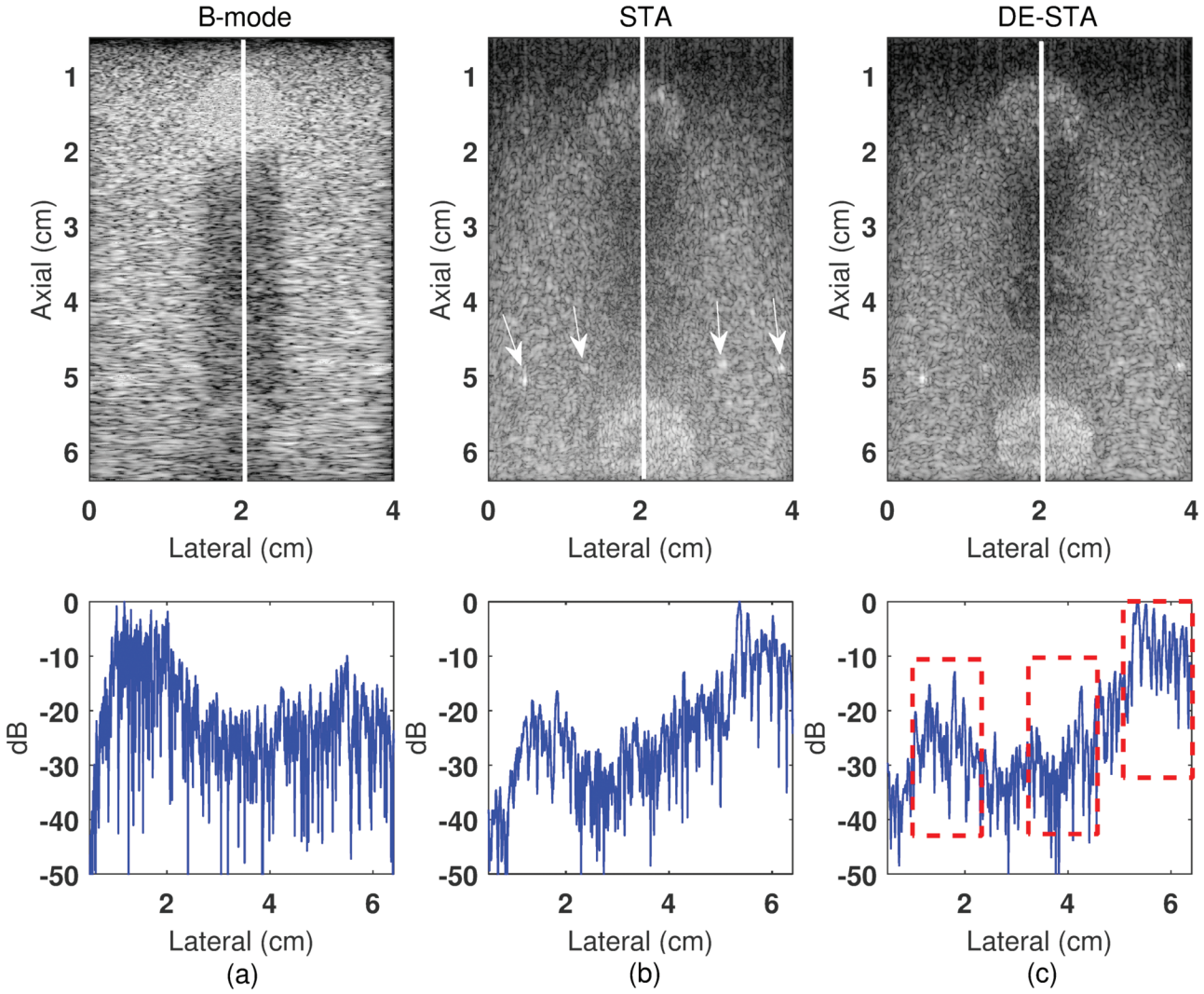

Fig. 8. Experimental log-envelope beamformed images obtained in (a) B-mode imaging, (b) traditional STA imaging, and (c) DE-STA imaging. Top row: phantom images. Bottom row: axial line plots at 2.0 cm (indicated by vertical white line). The white arrows in (b) indicate the locations of four wire targets. The dynamic ranges are (a) 40 dB; (b) and (c) 60 dB. Three dashed squares on axial line plots indicate the position of the hyper, hypo, and another hyper inclusions.

We used a band-pass filter to cut off the frequency components which are far from the central frequency to stabilize the inversion of coding matrices. DE-STA can also be combined with pseudo-inverse or other regularization methods [31] to inverse the encoding matrix more stably. The DE-STA technique can also be combined with temporal-encoding such as orthogonal Golay codes to further improve SNR in the future. The decoding methods proposed in this paper can be applied to the case when a different encoding matrix or different Δt_{li} is used, such as for B-mode, plane wave imaging, and synthetic aperture sequential beamforming. For the above methods, we just need to construct the corresponding delay matrix $\mathbf{T}$, and the decoding process and image reconstruction process will be similar as in DE-STA. Special attention should be paid to obtain a stable decoding process. Nevertheless, we expect that the decoding and image reconstruction framework proposed here can be applied to the image reconstruction using the pre-beamformed RF data obtained in B-mode and plane wave imaging to improve the image quality.

The main goal of this paper is to propose the theory of DE-STA, demonstrate its feasibility, and verify the improvement of the SNR of the pre-beamformed RF signals. Because there are several other approaches to improve the SNR of the pre-beamformed RF signals by using multi-element transmission, it would be an interesting future study to compare the performance of these approaches and B-mode with DE-STA in a systematic way.

V. Conclusion

This paper addresses the feasibility of a delay-encoded synthetic transmit aperture technique in ultrasound imaging. A unique coding matrix has been designed to encode the transmission scheme, which can be implemented in commercial clinic ultrasound scanners. The algorithm

was tested in both Field II simulations and experiments. The results from both simulations and experiments demonstrate increased SNR of pre-beamformed RF signals compared with traditional STA, which leads to enhanced image qualities such as spatial resolution, PSNR, and contrast in the DE-STA reconstructed images. The proposed image reconstruction framework may be also extended to B-mode, plane wave imaging, and synthetic aperture sequential beamforming.

Acknowledgments

We would like to thank our funding agencies: Natural Sciences and Engineering Research Council of Canada (NSERC), Canada Foundation for Innovation (CFI), and Ryerson University. We are grateful to Dr. R. Cobbold, Dr. J. Tavakkoli, A. Moghimi, and Y. Li for their valuable discussions and suggestions.

References

[1] R. S. C. Cobbold, *Foundations of Biomedical Ultrasound*. Toronto, Canada: Oxford University Press, 2007. 2006.
[2] J. A. Jensen, S. I. Nikolov, K. L. Gammelmark, and M. H. Pedersen, "Synthetic aperture ultrasound imaging," *Ultrasonics*, vol. 44, Supplement, vol. 12/22, pp. e5–e15, 2006.
[3] C. R. Hazard and G. R. Lockwood, "Effects of motion on a synthetic aperture beamformer for real-time 3D ultrasound," in *1999 IEEE Ultrasonics Symp. Proc.*, vol. 1 and 2, pp. 1221–1224.
[4] N. Bottenus, B. C. Byram, J. J. Dahl, and G. E. Trahey, "Synthetic aperture focusing for short-lag spatial coherence imaging," *IEEE Trans. Ultrason. Ferroelectr. Freq. Control*, vol. 60, no. 9, pp. 1816–1826, 2013.
[5] Y. Tasinkevych, Z. Klimonda, M. Lewandowski, A. Nowicki, and A. Lewin, "Modified multi-element synthetic transmit aperture method for ultrasound imaging: A tissue phantom study," *Ultrasonics*, vol. 53, no. 2, pp. 570–579, 2013.
[6] G. R. Lockwood, J. R. Talman, and S. S. Brunke, "Real-time 3-D ultrasound imaging using sparse synthetic aperture beamforming," *IEEE Trans. Ultrason. Ferroelectr. Freq. Control*, vol. 45, no. 4, pp. 980–988, 1998.
[7] Y. K. Chan and V. C. Koo, "An introduction to synthetic aperture radar (SAR)," in *Progress in Electromagnetics Research B*, 2008, pp. 27–60.
[8] C. Chang, Y. Chang, Y. Ma, and K. K. Shung, "Reliable estimation of virtual source position for SAFT imaging," IEEE Trans. Ultrason. Ferroelectr. Freq. Control, vol. 60, no. 2, pp. 356–363, 2013.
[9] J. T. Ylitalo and H. Ermert, "Ultrasound synthetic aperture imaging: Monostatic approach," *IEEE Trans. Ultrason. Ferroelectr. Freq. Control*, vol. 41, no. 3, pp. 333–339, 1994.
[10] Z. Li, Q. Chen, J. Zhou, and B. Tian, "Analysis of synthetic aperture radar image characteristics for seismic disasters in the Wenchuan earthquake," *J. Appl. Remote Sens.*, vol. 3, no. 1, art. no. 031685, 2009.
[11] L. Huang, Y. Labyed, K. Hanson, D. Sandoval, J. Pohl, and M. Williamson, "Detecting breast microcalcifications using super-resolution ultrasound imaging: A clinical study," in *Medical Imaging 2013: Ultrasonic Imaging, Tomography, and Therapy*, vol. 8675, art. no. 86751O, 2013.
[12] Y. Li and J. A. Jensen, "Synthetic aperture flow imaging using dual stage beamforming: Simulations and experiments," *J. Acoust. Soc. Am.*, vol. 133, no. 4, pp. 2014–2024, 2013.
[13] M. Karaman, P.-C. Li, and M. O'Donnell, "Synthetic aperture imaging for small scale systems," *IEEE Trans. Ultrason. Ferroelectr. Freq. Control*, vol. 42, no. 3, pp. 429–442, 1995.
[14] M. H. Bae, M. K. Jeong, T. K. Song, and Y. B. Ahn, "Experimental study of transmit synthetic focusing combined with receive dynamic focusing in B-mode ultrasound imaging systems," in *1999 IEEE Ultrasonics Symp. Proc., vols. 1 and 2*, pp. 1261–1264.
[15] M.-H. Bae and M.-K. Jeong, "A study of synthetic-aperture imaging with virtual source elements in B-mode ultrasound imaging systems," *IEEE Trans. Ultrason. Ferroelectr. Freq. Control*, vol. 47, pp. 1510–1519, 2000.
[16] F. Gran and J. A. Jensen, "Multi element synthetic aperture transmission using a frequency division approach," in *2003 IEEE Symp. on Ultrasonics*, vol. 2, pp. 1942–1946.
[17] F. Gran, J. A. Jensen, and B. Jakobsson, "A code division technique for multiple element synthetic aperture transmission," *Medical Imaging 2004: Ultrasonic Imaging and Signal Processing*, vol. 5373, pp. 300–306, 2004.
[18] C. H. Frazier and W. D. O'Brien, Jr., "Synthetic aperture imaging with a virtual source element," in *Proc. 1996 IEEE Ultrasonics Symp.*, vol. 2, pp. 1555–1558.
[19] J. Kortbek, J. A. Jensen, and K. L. Gammelmark, "Sequential beamforming for synthetic aperture imaging," *Ultrasonics*, vol. 53, no. 1, pp. 1–16, 2013.
[20] R. Y. Chiao, L. J. Thomas, and S. D. Silverstein, "Sparse array imaging with spatially-encoded transmits," in *1997 Proc. Ultrasonics Symp.*, vol. 2, pp. 1679–1682.
[21] R. Y. Chiao and L. J. Thomas, "Method and apparatus for ultrasonic synthetic transmit aperture imaging using orthogonal complementary codes," U.S. Patent 6048315 A, Apr. 11, 2000.
[22] R. Y. Chiao and L. J. Thomas, "Synthetic transmit aperture imaging using orthogonal Golay coded excitation," in *2000 IEEE Ultrasonics Symp. Proc.*, vol. 1 and 2, pp. 1677–1680.
[23] S. I. Nikolov and J. A. Jensen, "Comparison between different encoding schemes for synthetic aperture imaging," in *Medical Image 2002: Ultrasonic Imaging and Signal Processing*, vol. 4687, pp. 1–12, 2002.
[24] R. J. Zemp, A. Sampaleanu, and T. Harrison, "S-sequence encoded synthetic aperture B-scan ultrasound imaging," in *2013 IEEE Int. Ultrasonics Symp*, pp. 589–591.
[25] T. Harrison, A. Sampaleanu, and R. J. Zemp, "S-sequence spatially-encoded synthetic aperture ultrasound imaging," *IEEE Trans. Ultrason. Ferroelectr. Freq. Control*, vol. 61, no. 5, pp. 886–890, 2014.
[26] K. L. Gammelmark and J. A. Jensen, "Multi-element synthetic transmit aperture imaging using temporal encoding," in *Medical Image 2002: Ultrasonic Imaging and Signal Processing*, vol. 4687, pp. 25–36.
[27] J. A. Jensen and N. B. Svendsen, "Calculation of pressure fields from arbitrarily shaped, apodized, and excited ultrasound transducers," *IEEE Trans. Ultrason. Ferroelectr. Freq. Control*, vol. 39, no. 2, pp. 262–267, 1992.
[28] J. A. Jensen, "FIELD: A program for simulating ultrasound systems," *Med. Biol. Eng. Comput.*, vol. 34, suppl. 1, pt. 1, pp. 351–353, 1996.
[29] J. A. Jensen, O. Holm, L. J. Jensen, H. Bendsen, S. I. Nikolov, B. G. Tomov, P. Munk, M. Hansen, K. Salomonsen, J. Hansen, K. Gormsen, H. M. Pedersen, and K. L. Gammelmark, "Ultrasound research scanner for real-time synthetic aperture data acquisition," *IEEE Trans. Ultrason. Ferroelectr. Freq. Control*, vol. 52, no. 5, pp. 881–891, 2005.
[30] J. A. Jensen, H. Holten-Lund, R. T. Nilsson, M. Hansen, U. D. Larsen, R. P. Domsten, B. G. Tomov, M. B. Stuart, S. I. Nikolov, M. J. Pihl, Y. Du, J. H. Rasmussen, and M. F. Rasmussen, "SARUS: A synthetic aperture real-time ultrasound system," *IEEE Trans. Ultrason. Ferroelectr. Freq. Control*, vol. 60, no. 9, pp. 1838–1852, 2013.
[31] S. Gilbert, "The fundamental theorem of linear algebra," *Am. Math. Mon.*, vol. 100, pp. 848–859, Nov. 1993.

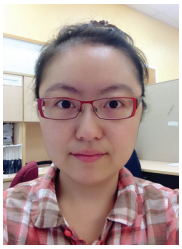

Ping Gong was born in Changchun, Jilin, China in 1987. She received the B.Sc. degree from Tianjin University, China, majoring in biomedical engineering, in 2010. She completed her M.Sc. degree in the Department of Electrical and Computer Engineering at Lakehead University, Canada in 2012. She has been pursuing her Ph.D. degree in biomedical physics at Ryerson University with Dr. Yuan Xu and Dr. Michael C. Kolios since 2012. Her research focuses on developing ultrasound transmission and beamforming algorithms to improve ultrasound image quality.

Michael C. Kolios was born in Toronto, Canada, and moved to Greece at a young age, finishing his high school studies in Athens, Greece. He completed a B.Sc. Hons. degree in physics, with a computer science minor, at the University of Waterloo in 1991. He subsequently completed his M.Sc. and Ph.D. degrees in the Department of Medical Biophysics at the University of Toronto in 1994 and 1998, respectively. In 1997, he joined the Department of Physics at Ryerson University, where he is now a full professor. He is the Associate Dean Research and Graduate Studies in the Faculty of Science. He held a Canada Research Chair in Biomedical Applications of Ultrasound (2004–2014) and has been the recipient of numerous awards for his research and teaching. His research interests include ultrasound/optical imaging and characterization of tissues and cells, high-frequency ultrasound imaging and spectroscopy, acoustic microscopy, ultrasound- and laser-based therapy, optical coherence tomography, and photoacoustic imaging. More information about his work can be found at http://www.physics.ryerson.ca/user/4.

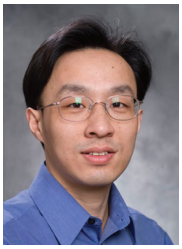

Yuan Xu was born in China in 1971. He received his Ph.D. degree in physics from the Institute of Physics, Chinese Academy of Sciences, Beijing, China, in 1999. He also received a Ph.D. degree in biomedical engineering from Texas A&M University, College Station, TX, USA, in 2003. Since 2005, he has been working in Ryerson University, Toronto, Canada. He is an Associate Professor in the Department of Physics. His research interests include the development of novel algorithms to improve the image qualities of ultrasound images and to reduce the cost of ultrasound imaging systems.